MDPI

Communication

Tuning the Catalytic Water Oxidation Activity through Structural Modifications of High-Nuclearity Mn-oxo Clusters [Mn$_{18}$M] (M = Sr^{2+}, Mn^{2+})

Joaquín Soriano-López *, Rory Elliott, Amal C. Kathalikkattil, Ayuk M. Ako and Wolfgang Schmitt *

School of Chemistry & SFI AMBER Centre, Trinity College, University of Dublin, 999014 Dublin, Ireland; relliot@tcd.ie (R.E.); amalcherian@gmail.com (A.C.K.); akomana12@gmail.com (A.M.A.)
* Correspondence: sorianoj@tcd.ie (J.S.-L.); schmittw@tcd.ie (W.S.)

Abstract: The water oxidation half-reaction is considered the bottleneck in the development of technological advances to replace fossil fuels with sustainable and economically affordable energy sources. In natural photosynthesis, water oxidation occurs in the oxygen evolving complex (OEC), a manganese-oxo cluster {Mn$_4$CaO$_5$} with a cubane-like topology that is embedded within a redox-active protein environment located in photosystem II (PS II). Therefore, the preparation of biomimetic manganese-based compounds is appealing for the development of efficient and inexpensive water oxidation catalysts. Here, we present the water oxidation catalytic activity of a high-nuclearity mixed-metal manganese-strontium cluster, [Mn$^{III}_{12}$Mn$^{II}_6$Sr(μ_4-O$_8$)(μ_3-Cl)$_8$(HL^{Me})$_{12}$(MeCN)$_6$]Cl$_2$·15MeOH (**Mn$_{18}$Sr**) (HL^{Me} = 2,6-bis(hydroxymethyl)-*p*-cresol), in neutral media. This biomimetic mixed-valence cluster features different cubane-like motifs and it is stabilized by redox-active, quinone-like organic ligands. The complex displays a low onset overpotential of 192 mV and overpotentials of 284 and 550 mV at current densities of 1 mA cm^{-2} and 10 mA cm^{-2}, respectively. Direct O$_2$ evolution measurements under visible light-driven water oxidation conditions demonstrate the catalytic capabilities of this cluster, which exhibits a turnover frequency of 0.48 s^{-1} and a turnover number of 21.6. This result allows for a direct comparison to be made with the structurally analogous Mn-oxo cluster [Mn$^{III}_{12}$Mn$^{II}_7$(μ_4-O)$_8$(μ_3-OCH$_3$)$_2$(μ_3-Br)$_6$(HL^{Me})$_{12}$(MeOH)$_5$(MeCN)]Br$_2$·9MeCN·MeOH (**Mn$_{19}$**), the water oxidation catalytic activity of which was recently reported by us. This work highlights the potential of this series of compounds towards the water oxidation reaction and their amenability to induce structural changes that modify their reactivity.

Keywords: water oxidation catalysis; oxygen evolution reaction; manganese; redox-active ligands; cubane-type structure; biomimetic catalyst; immobilized molecular catalyst

1. Introduction

Water oxidation catalysis has become a central focus area in the quest for replacing fossil fuel combustion for energy production by renewable and environmentally friendly energy sources [1,2]. Due to its ubiquity, water represents the ideal source of reducing equivalents to produce H$_2$ via the water splitting reaction, hence conceptually mimicking natural photosynthesis. This process provides the storage of clean energy in the form of chemical bonds with an intrinsic high gravimetric energy density [3–5]. However, the water oxidation half-reaction (Equation (1)) within this scheme is complex and highly energetically demanding. Therefore, it requires the use of water oxidation catalysts (WOCs) that alleviate the energy requirements associated with each of the steps in the reaction mechanism and accelerate the sluggish kinetics of the O−O bond formation [6–8]. Indeed, the lack of cost-effective WOCs hampers the generation of economically affordable H$_2$ that could compete with fossil fuels for energy production [5,9]. In this matter, Ru- and Ir-based materials are highly efficient catalysts; however, their large-scale application is unfeasible due to the scarcity and prohibitive cost of these metals [10,11]. Therefore,

earth-abundant-based materials with water oxidation catalytic capabilities have been explored in recent years [12,13]. A myriad of systems have been reported displaying diverse water oxidation activities, which comprise mono- or multinuclear organometallic molecular species [14,15], polyoxometalates [16–19], colloidal particles [20,21], homo- and heterometallic oxides [22–24], metal-organic frameworks [25,26] and even metal-free catalysts [27,28]. Moreover, heterogenization of molecular WOCs through their immobilization into solid supports enables the fabrication of hybrid systems that combine the high catalytic activity of molecular catalysts with the stability and recyclability of heterogeneous materials [29,30].

$$2H_2O \rightarrow O_2 + 4H^+ + 4e^- \ E^0 = 1.229 \text{ (V) vs. RHE at } 25°C \tag{1}$$

In nature, water oxidation occurs at the oxygen evolving complex (OEC), a $\{Mn_4CaO_5\}$ oxo-cluster embedded in a protein environment within photosystem II (PS II) [31–33]. The efficacy of this biological enzymatic system relies on effective charge separation and accumulation, and electron mobility mechanisms [34]. The $\{Mn_4CaO_5\}$ cluster uses water as the ultimate source of electrons and transfers them to a tyrosine residue Y161, which locates directly at the periphery of the cluster, and provides an oxidizable side-chain to recover the photoexcited chlorophyll P680* into its ground state through rapid electron injection [35]. Notably, the harsh water oxidation conditions constantly damage the OEC and its surroundings, the structural integrity of which is reconstituted via self-repair mechanisms to avoid the cessation of activity after 30 min [36].

Given the nature of the OEC, it is not surprising that research efforts have been directed to produce bioinspired Mn-based WOCs featuring multiple metallic centers [37–41]. These WOCs are appealing as they can facilitate multiple-electron redox processes by accumulating multiple charge equivalents through different metal centers in a single molecule and within a narrow potential range. In addition, Mn is a highly attractive element due to its high abundance in the Earth's crust, availability and low toxicity [42]. Unfortunately, the low stability of Mn-based WOCs under operando conditions is a common issue that leads to either the formation of catalytically active heterogeneous manganese oxide, thus precluding the proper characterization of the complex [43], or fast catalytic decay due to catalyst deactivation [44]. A series of dodecanuclear Mn-oxo clusters, $[Mn_{12}O_{12}(OAc)_{16-x}L_x(H_2O)_4]$ are especially interesting as they show amenability to replace the organic ligand (L) to modulate the WOC activity and solubility in aqueous solutions. For instance, when L = acetate, benzoate, benzenesulfonate, diphenylphosphonate or dichloroacetate, the clusters are water-insoluble and show poor WOC activity in the solid state, displaying high onset overpotentials between 640 and 820 mV. Maayan and co-workers demonstrated that employing redox-active di- or trihydroxybenzoate organic ligands increases the clusters' solubilities in aqueous solutions, allowing for the study of their WOC properties in the homogeneous phase [45,46]. These clusters displayed good catalytic activity and a reduced onset overpotential thanks to the non-innocent role of the quinone-like ligands. However, the oxygen evolution rate decreases gradually after one hour under an applied bias, indicating that catalyst deactivation is still a problem in these systems. Our group recently reported the activity of a bioinspired, high-nuclearity Mn-oxo cluster, $[Mn^{III}_{12}Mn^{II}_7(\mu_4\text{-}O)_8(\mu_3\text{-}OCH_3)_2(\mu_3\text{-}Br)_6(HL^{Me})_{12}(MeOH)_5(MeCN)]Br_2$ (**Mn₁₉**), which contains 2,6-bis(hydroxymethyl)-*p*-cresol, a non-innocent, redox-active ligand that resembles the tyrosine residue Y161 in PS II [47]. Importantly, **Mn₁₉**-modified carbon paste electrodes delivered high catalytic activity in neutral media, displaying 10 mA cm^{-2} and even 100 mA cm^{-2} at applied overpotentials of 482 and 654 mV, respectively. Despite the high activity shown by this cluster, we identified oxidation of the primary alcohols of the organic ligand as the main deactivation pathway leading to catalyst deactivation. All things considered, Mn-oxo clusters in general have shown potential towards water oxidation catalysis, but their stability issues must be addressed in the near future in order to obtain more durable catalysts before their commercial implementation is possible.

Interestingly, the nonadecanuclear Mn-oxo cluster (**Mn$_{19}$**) was initially investigated by Powell et al. due to its unprecedented ground spin state of S = 83/2 [48]. Thereafter, structural variants of this compound where the central Mn^{II} ion was replaced with various heterometals such Dy^{III}, Sr^{II}, Y^{III}, Cd^{II} and Lu^{III} provided a synthetic route for the [**Mn$_{18}$M**] family [24]. Additionally, in this work, the authors showed how weak antiferromagnetic interactions between magnetic units can be tuned using different diamagnetic metal centers.

Here, we report the heterogeneous water oxidation catalytic activity at pH = 7.2 of [Mn$^{III}_{12}$Mn$^{II}_6$Sr(μ_4-O$_8$)(μ_3-Cl)$_8$(HL^{Me})$_{12}$(MeCN)$_6$]Cl$_2$·15MeOH (**Mn$_{18}$Sr**), a bioinspired, high-nuclearity Mn-oxo cluster which is analogous to the previously reported **Mn$_{19}$** complex. As part of a modified carbon paste electrode, **Mn$_{18}$Sr** displays an onset overpotential of 192 mV and achieves a current density of 10 mA cm^{-2} at 550 mV. Post-catalytic characterization indicates that **Mn$_{18}$Sr** is the true catalyst under the examined experimental conditions and that it follows the same, or a very similar, deactivation pathway than that found for the **Mn$_{19}$** complex. Additionally, light-induced water oxidation experiments confirm O$_2$ evolution promoted by **Mn$_{18}$Sr**, revealing a TOF of 0.48 s^{-1} and a maximum TON of 21.6. **Mn$_{18}$Sr** is a mixed-valence, polynuclear Mn complex stabilized by redox-active, tridentate 2,6-bis(hydroxymethyl)-*p*-cresol (H$_3$L^{Me}) ligands featuring different cubane motifs, which are organized to form a supertetrahedral structure (Figure 1). Within this structure, **Mn$_{18}$Sr** displays cubane-like {Mn$_7$Cl$_2$O$_7$} clusters containing 7-coordinated 'dangling' Mn^{II} atoms that are assumed to act as the catalytically active centers. Additionally, the presence of Sr^{II} is also intriguing, as this is the only metal known which can replace Ca^{II} in the OEC without rendering the cluster catalytically inactive [49]. Moreover, in a recent study by Mameri et al., **Mn$_{18}$Sr** and **Mn$_{19}$** were successfully employed in the electrocatalytic oxidation of benzyl alcohol into benzaldehyde using O$_2$ as an oxidant and TEMPO (2,2,6,6-tetramethylpiperidine-1-oxyl) as a co-catalyst [50]. Therefore, given the previously reported high WOC activity for the homologous **Mn$_{19}$** cluster, its resemblance with the OEC, its insolubility in aqueous solutions and facile preparation from inexpensive and environmentally benign starting materials, **Mn$_{18}$Sr** is an attractive candidate for heterogeneous H$_2$O oxidation catalysis.
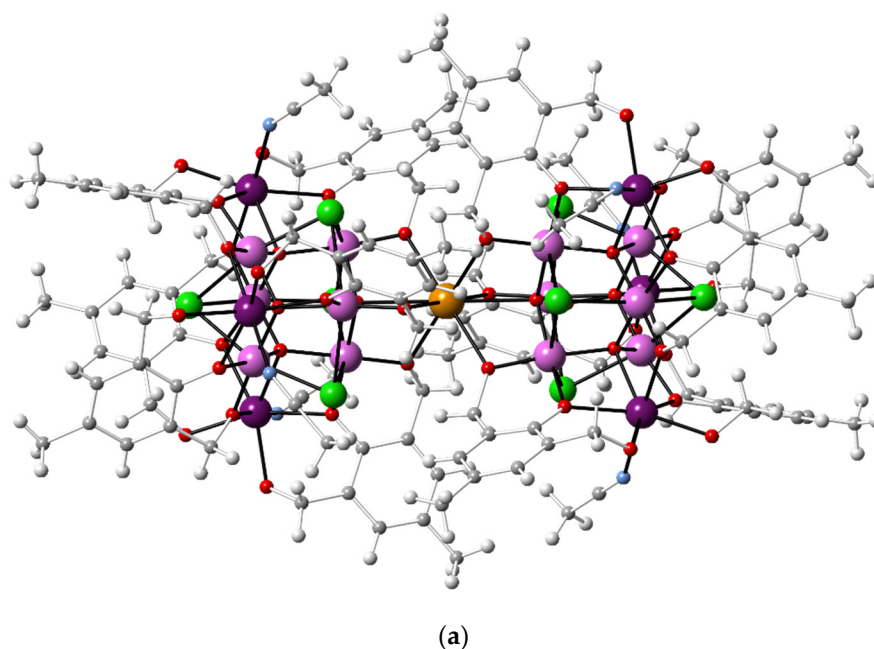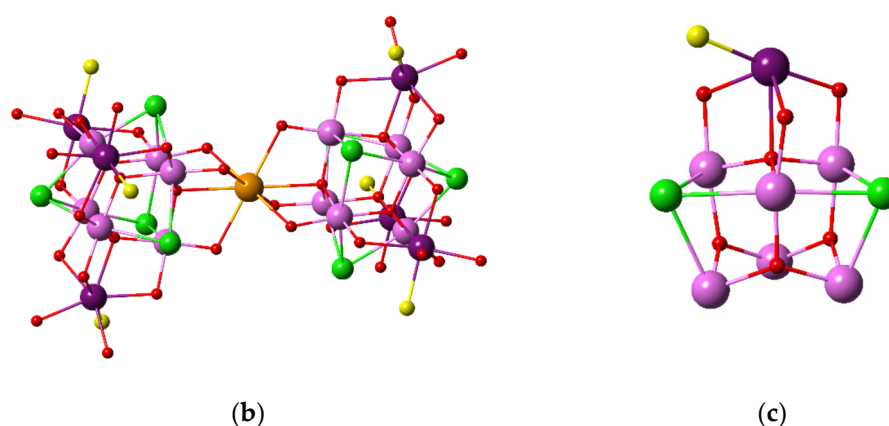

(**a**)

Figure 1. *Cont.*

(b)   **(c)**

Figure 1. Single crystal X-ray structure of **Mn₁₈Sr**. (**a**) Molecular structure of [$Mn^{III}_{12}Mn^{II}_6Sr(\mu_4$-$O_8)(\mu_3$-$Cl)_8(HL^{Me})_{12}(MeCN)_6]^{2+}$ (**Mn₁₈Sr**). (**b**) Core structure of **Mn₁₈Sr** in which the organic ligands have been omitted for clarity. (**c**) Detail of the cubane-like {$Mn_7Cl_2O_7$} cluster containing a 7-coordinated 'dangling' Mn^{II} atom in the {$Mn^{III}_6Mn^{II}_4$} core of **Mn₁₈Sr**. Color code: Mn^{II} (purple), Mn^{III} (pink), Sr (orange), Cl (green), C (gray), O (red), N (blue) and H (white); solvent position in (**b**,**c**) are shown as yellow spheres.

2. Materials and Methods

All chemicals and solvents were used as purchased without further purification. The Mn and Sr salts precursors were purchased from abcr GmbH (Karlsruhe, Germany), whereas the rest of precursors were purchased from Sigma-Aldrich Ltd. (Gillingham, United Kingdom). The modified carbon paste electrodes were prepared using ALS Co. Ltd. (Tokyo, Japan), CPO Carbon Paste Oil.

Synthesis of [$Mn^{III}_{12}Mn^{II}_6Sr(\mu_4$-$O)_8(\mu_3$-$Cl)_8(HL^{Me})_{12}(MeCN)_6]Cl_2\cdot15MeOH$ (Mn₁₈Sr):

The synthesis of **Mn₁₈Sr** was performed following a previously reported procedure [50]. $MnCl_2\cdot4H_2O$ (0.2 g, 1 mmol), Et_3N (0.1 g, 1 mmol) and 2,6-bis(hydroxymethyl)-4-methylphenol (H_3L^{Me}) (0.17 g, 1 mmol) were added into a solvent mixture of MeCN and MeOH (25 mL/5 mL) and stirred for 30 min at room temperature. Then, $Sr(NO_3)_2$ (0.11 g, 0.5 mmol, 0.5 equiv.) was added. The resulting mixture was stirred for an additional 1 h and then refluxed for 2 h. The dark brown mixture was cooled, filtered and left to crystallize at room temperature. Dark brown crystals of **Mn₁₈Sr** were obtained after 24 h of slow evaporation. The title compound was characterized by FT-IR (Figure S1a), which matched that of the previously reported **Mn₁₈Sr**, and by Raman spectroscopy (Figure S2a).

Synthesis of [$Mn^{III}_{12}Mn^{II}_7(\mu_4$-$O)_8(\mu_3$-$OCH_3)_2(\mu_3$-$Br)_6(HL^{Me})_{12}(MeOH)_5(MeCN)$] $Br_2\cdot9MeCN\cdot MeOH$ (Mn₁₉):

The synthesis of **Mn₁₉** was performed following a previously reported procedure [47]. $MnBr_2\cdot4H_2O$ (0.3 g, 1.4 mmol), Et_3N (0.18 g, 1.79 mmol) and 2,6-bis(hydroxymethyl)-4-methylphenol (H_3L^{Me}) (0.17 g, 1 mmol) were added into a solvent mixture of MeCN and MeOH (30 mL/5 mL). The reaction mixture was then stirred for 2 h at 30 °C and then refluxed for 1 h. Next, the reaction mixture was cooled at room temperature, filtered to remove insoluble components and left to crystallize by slow evaporation. Uniform single-crystals of **Mn₁₉** formed within a few days. The title compound was characterized by FT-IR (Figure S1b), which matched that of the previously reported **Mn₁₉**, and by Raman spectroscopy (Figure S2c).

Synthesis of the PS Complex [$Ru(bpy)_2(deeb)](PF_6)_2$:

The PS [$Ru(bpy)_2(deeb)](PF_6)_2$ was prepared in a three-step synthesis (summarized in Scheme 1) according to adapted literature protocols outlined by Ma et al. [51] and Meyer et al. [52].
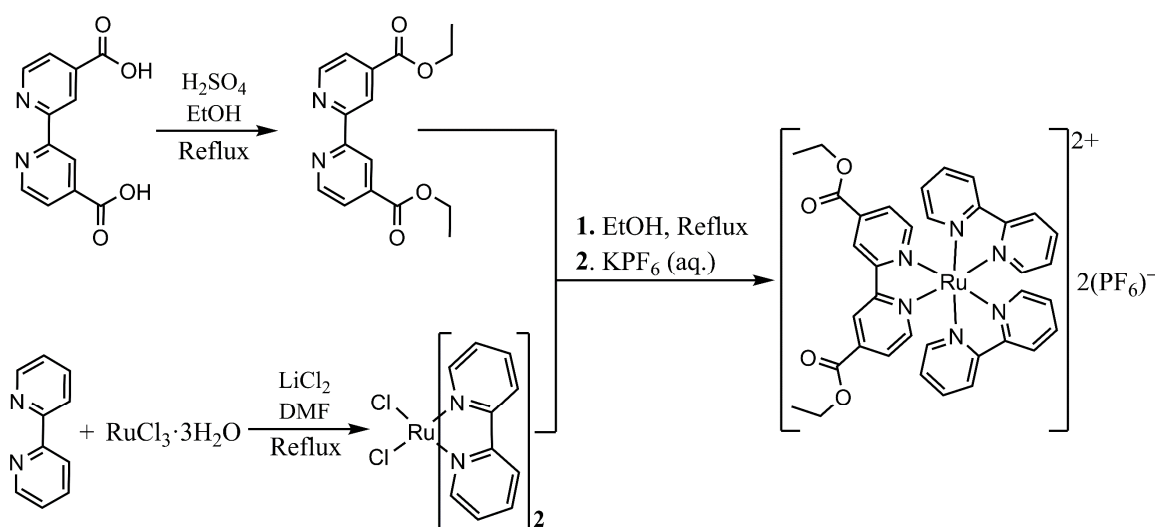
Scheme 1. Three-step synthetic route to afford the formation of the heteroleptic polypyridyl PS [Ru(bpy)$_2$(deeb)](PF$_6$)$_2$.

Diethyl 2,2′-bipyridine-4,4′-dicarboxylate (deeb) was synthesized according to a modified literature procedure outlined by Ma et al. [51]. Initially, 2,2′-bipyridine-4,4′-dicarboxylic acid (0.30 g, 1.228 mmol) and concentrated H$_2$SO$_4$ (1 mL) were refluxed in EtOH (10 mL) for 4 h. The reaction mixture was then allowed to cool to room temperature and distilled water (30 mL) was added. The resulting white precipitate was then collected by filtration and washed with MeOH before drying under vacuum. The yield was 0.28 g, 1.02 mmol, 82%.

The ruthenium polypyridine precursor [Ru(bpy)$_2$]Cl$_2$ was synthesized according to an adapted literature procedure outlined by Meyer et al. [52]. RuCl$_3$·3H$_2$O (2.00 g, 7.649 mmol), bpy (2.39 g, 15.298 mmol) and LiCl (2.15 g, 50.715 mmol) were refluxed together in reagent grade DMF (14 mL) for 8 h. The reaction mixture was then cooled to 0 °C, causing the product to precipitate which was subsequently collected by filtration. The black crystalline product obtained was then washed with distilled H$_2$O (3 × 10 mL) followed by diethyl ether (3 × 10 mL) before allowing the product to dry in air. The yield was 1.593 g, 3.290 mmol, 43%.

The polypyridyl PS [Ru(bpy)$_2$(deeb)](PF$_6$)$_2$ was synthesized according to an adapted literature procedure described by Ma et al. [51]. Ru(bpy)$_2$Cl$_2$ (38.0 mg, 0.08 mmol) and deeb (50.0 mg, 0.16 mmol) were refluxed in EtOH (10 mL) under an atmosphere of nitrogen for 48 h. The solvent was then evaporated under reduced pressure, and the resulting residue was recrystallized from an aqueous saturated KPF$_6$ solution to afford the formation [Ru(bpy)$_2$(deeb)](PF$_6$)$_2$ as a red powder. The yield was 60.1 mg, 0.057 mmol, 69%.

Electrocatalytic Water Oxidation: Electrochemical measurements were performed with a Biologic VSP potentiostat. Ohmic drop was compensated prior to each experiment using the positive feedback compensation method as implemented in the instrumental setup. A three-electrode set-up was used comprising a Saturated Calomel Electrode (SCE) reference electrode, carbon paste (CP) working electrode and a Pt wire counter electrode (alternatively, a Pt mesh was employed for bulk water electrolysis experiments). The CP working electrodes employed for cyclic voltammetry (CV) and bulk water electrolysis had a surface area of 0.02 cm^2, whereas those employed for linear sweep voltammetry (LSV) had a surface area of 0.07 cm^2. These surface areas were employed to calculate the current densities. To prepare **Mn$_{18}$Sr**-modified CP working electrodes (**Mn$_{18}$Sr**/CP), **Mn$_{18}$Sr** was blended with CP at a 30% weight ratio (30 wt %). Then, the resulting mixture was inserted inside the CP electrode pocket. All the measurements were carried out in a 50 mM potassium phosphate (KP$_i$) buffer solution with KNO$_3$ (1 M) as electrolyte at pH 7.2. An ALS RRDE-3A set-up with a CP rotating disc electrode was used for the LSV measurements at 1600 r.p.m., and at a scan rate of 10 mV s^{-1}. Tafel data was extracted from

these LSV experiments and the onset overpotential was estimated from the intersection point between the tangent line of the Faradaic current at 1 mA cm^{-2} and the non-Faradaic current. Chronopotentiometry at applied current densities of 1 mA cm^{-2} and 10 mA cm^{-2} were performed in an H-cell where the working and reference electrodes were separated from the counter electrode by a glass frit (P0). For these chronopotentiometric experiments, the CP working electrode surface was covered with 4 μL of Nafion 117 solution using a micropipette and dried at room temperature.

All the applied potentials (E_{app}) were converted to the NHE reference scale using:

$$E_{NHE} = E_{SCE} + 0.241 \; (V) \tag{2}$$

The overpotentials (η) were calculated by subtracting the thermodynamic water oxidation potential $E^0_{H_2O/O_2}$ from E_{app} as:

$$\eta = E_{app} - E^0_{H_2O/O_2} \tag{3}$$

where $E^0_{H_2O/O_2}$ was pH-corrected employing the Nernst equation:

$$E^0_{H_2O/O_2} = 1.229 - (0.059 \times pH) \; (V) \text{ vs. NHE at 25 °C} \tag{4}$$

Light-Induced Water Oxidation Catalysis: Oxygen evolution was measured using a Unisense oxygen sensor (Clark electrode, OX-NP model). The microsensor was connected to a monomer and a computer operating the SensorTrace Suite software package. A two-point calibration method was employed prior to the measurements, using (a) a zero-oxygen determination of an anoxic aqueous solution (prepared using a mixture of NaOH and sodium ascorbate) and (b) air-saturated distilled water at a known temperature (prepared by vigorously bubbling air for 10 min into the Unisense calibration chamber (CAL300). Light-driven O_2 evolution experiments were carried out using a Prizmatix LED light (λ = 470 nm), connected to a fiber optic cable. The light intensity of the incident radiation at the center of the reactor was determined to be 10 mW cm^{-2}. The operating distance between the fiber optic tip and the reaction vessel was 1 cm.

Typically, [Ru(bpy)$_2$(deeb)](PF$_6$)$_2$ (deeb = 4,4-di(ethoxycarbonyl)-2,2-bipyridine) (2.00 mg, 0.47 mM) as a photosensitizer (PS) and Na$_2$S$_2$O$_8$ (11.9 mg, 10 mM) as sacrificial electron acceptor (SEA) were loaded into a crimp vial, which was then sealed with a butyl-rubber septum and covered with aluminum foil to prevent early reaction. Two 0.1 mg/mL catalysts stock solution were prepared by dispersing either **Mn$_{18}$Sr** or **Mn$_{19}$** in a 10 mM NaP$_i$ buffer aqueous solution at pH 7.0. For comparison of the water oxidation catalytic activity of these two catalysts, we employed 5 nmol of either **Mn$_{18}$Sr** or **Mn$_{19}$** in the experiments by injecting the corresponding volume of the stock solution into the vial. The final volume of the mixture was adjusted to 5 mL by the addition of NaP$_i$ buffer solution. The OX-NP Clark electrode (Unisense) and grounding cable were inserted into the solution phase through the septum and the real-time O_2 quantities were monitored thereafter. The aqueous mixture was then de-aerated by bubbling N$_2$ in the vial for several minutes, before removing the N$_2$ inlet and waiting for a consistent, steady O_2 reading. At this point, the content of the vial was illuminated whilst the O_2 concentration in solution was monitored in real time.

The turnover numbers (TON) and initial turnover frequencies (TOF) were calculated as follows:

$$TON = \frac{n_{O_2}}{n_{catalyst}} \tag{5}$$

$$TOF = \frac{n_{O_2}}{n_{catalyst} \times time} \tag{6}$$

where n_{O_2} is the number of moles of O_2 produced, $n_{catalyst}$ is the number of moles of catalyst employed and the time period considered was 10 s after the onset of the O_2 evolution.

3. Results

Heterogeneous water oxidation electrocatalytic experiments were performed using **Mn₁₈Sr**-modified carbon paste (CP) working electrodes, where the **Mn₁₈Sr** weight ratio (wt %) in the CP blend was kept at 30% (**Mn₁₈Sr**/CP). An SCE reference electrode and a Pt wire (or mesh) counter electrode completed the three-electrode set-up. These measurements were conducted in a 50 mM phosphate (KP$_i$) buffer at pH 7.2 using KNO$_3$ (1 M) as electrolyte.

Initial cyclic voltammetry (CV) using the **Mn₁₈Sr**/CP electrodes shows increasing current densities at oxidative potentials that clearly contrast with the catalyst-free CP electrodes (blank), indicating the appearance of a multielectron transfer catalytic process (Figure 2a). Is worth mentioning that a crossover loop process appears at the firsts CV cycles. This behavior corresponds to the redox activity of the organic *p*-cresol type (HL^{Me})$^{2-}$ ligand stabilizing the **Mn₁₈Sr** cluster as we previously demonstrated, and it arises from the partial ligand oxidation to form semihydroquinone, semiquinone or carboxylate derivatives [47]. The electrocatalytic activity and kinetics of the **Mn₁₈Sr**/CP electrodes were further investigated by linear sweep voltammetry (LSV). Figure 2b shows the performance of **Mn₁₈Sr**/CP, which reaches current densities of 1 mA cm^{-2} and 10 mA cm^{-2} at 284 and 550 mV of overpotential, respectively. Moreover, these electrodes show a remarkably low onset overpotential (η_{onset}) of 192 mV (Figure S3). The LSV data were employed to study the kinetics of the electrode using a Tafel plot (Figure 2c). **Mn₁₈Sr**/CP shows a slope of 220 mV dec^{-1} at low overpotentials, which increases to 260 mV dec^{-1} at >300 mV overpotentials. These slope values are higher than the typical Tafel slopes, suggesting that the kinetics of the electrode are limited by a diffusion process and electron transfer. Moreover, organic ligand oxidation may be competing with the water oxidation reaction.

In comparison with the catalytic activity previously reported by the **Mn₁₉** cluster, **Mn₁₈Sr** shows a reduction of ca. 60 mV in the onset overpotential. We also observe a slight decrease of ca. 10 mV in the overpotential needed to reach 1 mA cm^{-2}. However, due to its increased Tafel slope, **Mn₁₈Sr** displays current densities of 10 mA cm^{-2} and 100 mA cm^{-2} at higher overpotentials than **Mn₁₉** (see Table 1 and Figure 2d).

Table 1. Comparison of the electrocatalytic water oxidation performed by 30% **Mn₁₈Sr**/CP [1] and 30% **Mn₁₉**/CP electrodes.

	30% Mn₁₈Sr/CP	30% Mn₁₉/CP [2]
η_{onset} [3] (mV)	192	255
η [4] (mV) @ j = 1 mA cm^{-2}	284	296
η (mV) @ j = 10 mA cm^{-2}	550	482
η (mV) @ j = 100 mA cm^{-2}	827	654
Tafel slope (mV dec^{-1})	220/260	205

[1] Carbon Paste; [2] Data obtained from reference [47]; [3] Onset overpotential; [4] Overpotential at the given current density.

The stability of the **Mn₁₈Sr**/CP electrodes was investigated with repetitive CV and chronopotentiometric experiments. Repetitive CV measurements show that after 10 CV cycles, the activity of the **Mn₁₈Sr**/CP decays, suggesting that the catalyst slowly decomposes to a catalytically inactive species (Figure 3a). Moreover, the water oxidation catalytic activity decay is accompanied by the appearance of a pale brown precipitate on the electrode surface. We already observed this same behavior when employing **Mn₁₉**/CP electrodes and identified the new inactive species as amorphous manganese-potassium carbonate-phosphate species. We characterized the pale brown precipitate obtained with the **Mn₁₈Sr**/CP electrodes by Raman spectroscopy. Figure S2b shows the Raman spectra of this precipitate features only two bands that originate from carbon vibrations at 712 and 1049 cm^{-1}. This result is analogous to the one found for **Mn₁₉**/CP electrodes (Figure S2d), where we identify the **Mn₁₉** cluster as the true active species whereas oxidation of the primary alcohols of the *p*-cresol type ligand was identified as the main catalyst deactivation pathway. Therefore, given the similar behavior to **Mn₁₉**/CP electrodes, we can conclude

that under the tested conditions, **Mn₁₈Sr**, or a species closely related, must act as the true catalytically active species before it undergoes deactivation.

Consistent with the repetitive CV study, we observe a decrease in the WOC activity over time during the chronopotentiometric experiments (Figure 3b). It is important to note that for these experiments, we followed a common procedure to cover the electrode surface with a Nafion film [53]. The Nafion polymer acts as a proton shuttle transferring the protons generated at the electrode during the proton-coupled electron transfer (PCET) [54] events to the bulk and increases the mechanical stability of the CP electrodes. The **Mn₁₈Sr**/CP electrodes show relatively good stability for one hour at applied current densities of 1 mA cm^{-2} and 10 mA cm^{-2}, with initial overpotentials of 280 and 550 mV, respectively. The displayed overpotentials slightly increase over time, suggesting catalyst deactivation, which is not surprising given the low stability performed by Mn-oxo clusters under operando conditions. In fact, restarting the chronopotentiometry at an applied current density of 1 mA cm^{-2} after ca. 80 min does not recover the initial performance of the electrode. Therefore, the applied overpotentials needed to reach current densities of 1 mA cm^{-2} and 10 mA cm^{-2} increase ca. 100 mV after 10 and 3 h, respectively (see Figure S4).
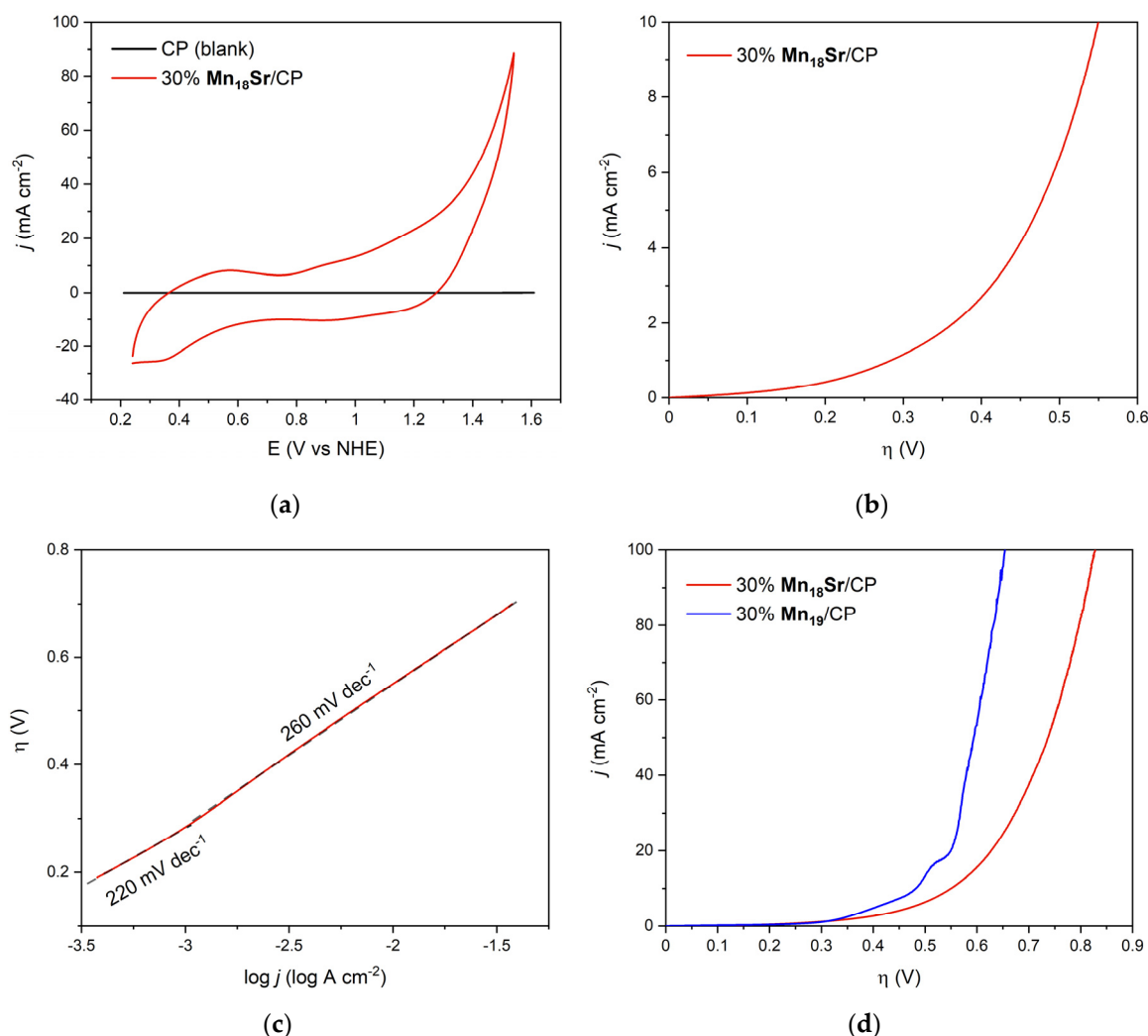

(a)

(b)

(c)

(d)

Figure 2. Water oxidation electrocatalytic activity of 30% **Mn₁₈Sr**/CP working electrodes performed in a 50 mM KP$_i$ aqueous buffer at pH = 7.2 using KNO₃ (1 M) as electrolyte. (**a**) Cyclic voltammograms comparing **Mn₁₈Sr**/CP (red) versus catalyst-free CP (black) electrodes. (**b**) Linear sweep voltammetry. (**c**) Tafel plot. The red line shows the data extracted from the LSV measurement, while the black dashed lines highlight the two different Tafel slopes. (**d**) Linear sweep voltammetry of a 30% **Mn₁₈Sr**/CP working electrode (red) compared to that of a 30% **Mn₁₉**/CP working electrode (blue).
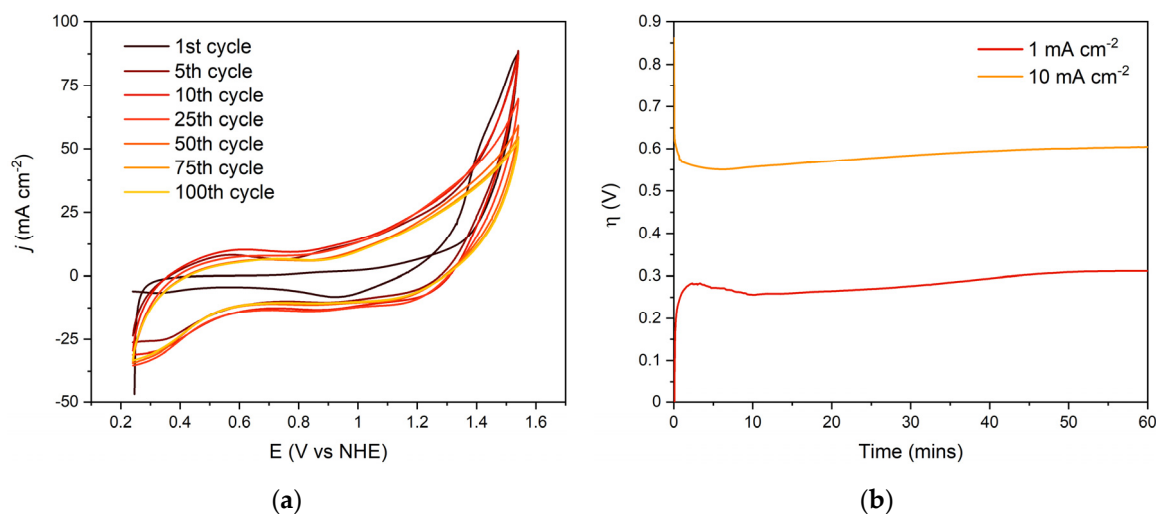
Figure 3. Stability tests of the 30% **Mn₁₈Sr**/CP working electrodes. (**a**) Evolution of the cyclic voltammogram over 100 cycles. (**b**) Chronopotentiometry measurements at applied current densities of 1 mA cm^{-2} (red) and 10 mA cm^{-2} (orange). The experiments were performed in a 50 mM KP$_i$ aqueous buffer at pH = 7.2 using KNO₃ (1 M) as electrolyte.

Finally, the oxygen evolution promoted by **Mn₁₈Sr** was confirmed under light-driven water oxidation conditions by employing a well-known protocol [55]. In this system, [Ru(bpy)₂(deeb)](PF₆)₂ was used as a PS and Na₂S₂O₈ as SEA within a 5 nmol **Mn₁₈Sr** suspension in 5 mL of 10 mM NaP$_i$ buffer aqueous solution at pH = 7. The O₂ evolved upon light irradiation (LED lamp, λ = 470 nm) was monitored employing a Clark electrode and compared with that of the analogous **Mn₁₉** under the same experimental conditions.

Figure 4 shows the O₂ evolution profiles displayed by both catalysts where the generated O₂ quantity continuously rises after the mixture is irradiated and reaches a plateau after ca. 120 s. The **Mn₁₉** cluster delivers an overall better catalytic activity with slightly superior kinetics than **Mn₁₈Sr**, which is in good agreement with the electrocatalytic experiments shown above. Hence, **Mn₁₉** reaches a turnover number (TON) of 25.8 and a turnover frequency (TOF) of 0.53 s^{-1}, whereas **Mn₁₈Sr** shows a TON of 21.6 and a TOF of 0.48 s^{-1}.
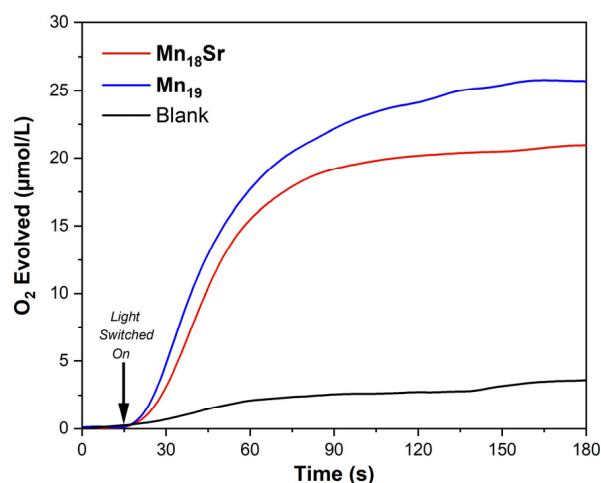

Figure 4. Kinetic monitoring (Clark electrode) of the light-driven O₂ evolution response of **Mn₁₈Sr** (red) and **Mn₁₉** (blue). Conditions: 5 nmol WOC loading in a 10 mM NaP$_i$ buffered aqueous solution (5 mL, initial pH = 7) containing Na₂S₂O₈ SEA (10 mM) and [Ru(bpy)₂(deeb)](PF₆)₂ PS (2 mg, 2.33 μmol). Irradiated using an LED lamp (λ = 470, 10 mW cm^{-2}). The mixture was stirred at a constant rate of 500 rpm and maintained at 25 °C by immersing the reaction vessel in a water bath.

4. Discussion

The exceptional OER activities observed using **Mn₁₈Sr** and **Mn₁₉** could stem from several shared structural features. For example, both compounds comprise high-nuclearity cluster cores, allowing the four electrons which must be abstracted from H_2O to promote O_2 evolution to be distributed between either eighteen or nineteen redox-active Mn centers in **Mn₁₈Sr** or **Mn₁₉**, respectively. This difference could underlie the marginally superior O_2 evolution activity displayed by **Mn₁₉** in comparison to **Mn₁₈Sr**. In addition, each cluster contains twelve Mn^{III} centers, which are integral to catalytic H_2O oxidation in many WOCs including the OEC of PS II. Furthermore, the geometric configurations of the Mn-oxo clusters **Mn₁₈Sr** and **Mn₁₉** resemble the OEC: two pseudocubane motifs appended by 'dangling' Mn^{II} centers, which are coordinated by terminal, labile solvent molecules, constitute a total of six substrate-accessible active sites per cluster. Finally, the presence of redox-active O-donor ligands which stabilize the cores structures of **Mn₁₈Sr** and **Mn₁₉** represents an additional parallel between these clusters and the OEC. Further research directions may include the replacement of the redox-active ligand to increase the stability of the clusters, which could also improve their water oxidation catalytic performance. Moreover, DFT calculations will help elucidate the WOC reaction mechanisms performed by these clusters to pinpoint key structure–reactivity relationships, and to disclose the role and stability of the redox-active quinone-like organic ligands.

5. Conclusions

In summary, we have shown the WOC activity in neutral media of a mixed-valence, high-nuclearity Mn-oxo cluster containing redox-active ligands, $[Mn^{III}_{12}Mn^{II}_6Sr(\mu_4\text{-}O_8)(\mu_3\text{-}Cl)_8(HL^{Me})_{12}(MeCN)_6]Cl_2 \cdot 15MeOH$ (**Mn₁₈Sr**), and compared with that of the analogous $[Mn^{III}_{12}Mn^{II}_7(\mu_4\text{-}O)_8(\mu_3\text{-}OCH_3)_2(\mu_3\text{-}Br)_6(HL^{Me})_{12}(MeOH)_5(MeCN)]Br_2 \cdot 9MeCN \cdot MeOH$ (**Mn₁₉**) complex under the same working conditions. As part of a modified carbon paste working electrode, **Mn₁₈Sr** shows good water oxidation electrocatalytic activity with a low onset overpotential of 192 mV. Moreover, the **Mn₁₈Sr**-modified electrodes display relatively low overpotentials of 284 and 550 mV at current densities of 1 mA cm^{-2} and 10 mA cm^{-2}, respectively. Unsurprisingly, the catalytic activity of this Mn-oxo cluster decays over time, where the organic ligand oxidation is identified as the main catalyst deactivation pathway. Moreover, the catalytically inactive species that appear after catalyst deactivation has been identified as a manganese-potassium carbonate-phosphate species. Importantly, these results are in good agreement with our previous investigations employing the **Mn₁₉** compound. Under light-induced water oxidation conditions, **Mn₁₈Sr** promotes O_2 evolution upon light irradiation, displaying an initial TOF of 0.48 s^{-1} and a maximum TON of 21.6. Overall, the **Mn₁₉** cluster displays an improved WOC activity than **Mn₁₈Sr** due to its faster kinetics.

Our results confirm the potential of this family of high-nuclearity Mn-oxo clusters as WOCs and highlights their amenability to structural modifications to tune their electronic properties and modulate their reactivity.

Supplementary Materials: The following are available online at https://www.mdpi.com/article/10.3390/w13152042/s1, Figure S1: FT-IR spectra of the freshly prepared **Mn₁₈Sr** (**a**) and **Mn₁₉** (**b**) complexes, Figure S2: Comparison of the Raman spectra obtained for the freshly developed **Mn₁₈Sr** (**a**) and **Mn₁₉** (**c**) complexes, and that for the recovered decomposition products identified as a catalytically inactive amorphous manganese-potassium carbonate-phosphate species (**b**,**d**), Figure S3: Calculation of the onset overpotential employing 30% **Mn₁₈Sr**/CP working electrodes. The onset overpotential was estimated from the intersection point between the tangent line of the Faradaic current at 1 mA cm^{-2} and the extrapolated line arising from the non-Faradaic current, Figure S4: Long-term chronopotentiometry measurements at applied current densities of (**a**) 1 mA cm^{-2} (red) and (**b**) 10 mA cm^{-2} (orange). The experiments were performed in an H-cell using a 50 mM KP$_i$ aqueous buffer at pH = 7.2 using KNO_3 (1 M) as electrolyte.

References

1. Zahran, Z.N.; Tsubonouchi, Y.; Mohamed, E.A.; Yagi, M. Recent advances in the development of molecular catalyst-based anodes for water oxidation toward artificial photosynthesis. *ChemSusChem* **2019**, *12*, 1775–1793. [CrossRef]
2. Li, J.; Triana, C.A.; Wan, W.; Adiyeri Saseendran, D.P.A.; Zhao, Y.; Balaghi, S.E.; Heidari, S.; Patzke, G.R. Molecular and heterogeneous water oxidation catalysts: Recent progress and joint perspectives. *Chem. Soc. Rev.* **2021**, *50*, 2444–2485. [CrossRef]
3. Sherif, S.A.; Barbir, F.; Veziroglu, T.N. Wind energy and the hydrogen economy—Review of the technology. *Sol. Energy* **2005**, *78*, 647–660. [CrossRef]
4. Mazloomi, K.; Gomes, C. Hydrogen as an energy carrier: Prospects and challenges. *Renew. Sustain. Energy Rev.* **2012**, *16*, 3024–3033. [CrossRef]
5. McKone, J.R.; Lewis, N.S.; Gray, H.B. Will solar-driven water-splitting devices see the light of day? *Chem. Mater.* **2014**, *26*, 407–414. [CrossRef]
6. Soriano-López, J.; Schmitt, W.; García-Melchor, M. Computational modelling of water oxidation catalysts. *Curr. Opin. Electrochem.* **2018**, *7*, 22–30. [CrossRef]
7. Dau, H.; Zaharieva, I. Principles, efficiency, and blueprint character of solar-energy conversion in photosynthetic water oxidation. *Acc. Chem. Res.* **2009**, *42*, 1861–1870. [CrossRef] [PubMed]
8. Zhang, X.-P.; Wang, H.-Y.; Zheng, H.; Zhang, W.; Cao, R. O–O bond formation mechanisms during the oxygen evolution reaction over synthetic molecular catalysts. *Chin. J. Catal.* **2021**, *42*, 1253–1268. [CrossRef]
9. Lyons, M.E.G.; Doyle, R.L.; Browne, M.P.; Godwin, I.J.; Rovetta, A.A.S. Recent developments in electrochemical water oxidation. *Curr. Opin. Electrochem.* **2017**, *1*, 40–45. [CrossRef]
10. Blakemore, J.D.; Crabtree, R.H.; Brudvig, G.W. Molecular catalysts for water oxidation. *Chem. Rev.* **2015**, *115*, 12974–13005. [CrossRef]
11. McCrory, C.C.L.; Jung, S.; Ferrer, I.M.; Chatman, S.M.; Peters, J.C.; Jaramillo, T.F. Benchmarking hydrogen evolving reaction and oxygen evolving reaction electrocatalysts for solar water splitting devices. *J. Am. Chem. Soc.* **2015**, *137*, 4347–4357. [CrossRef] [PubMed]
12. Galán-Mascarós, J.R. Water oxidation at electrodes modified with earth-abundant transition-metal catalysts. *ChemElectroChem* **2015**, *2*, 37–50. [CrossRef]
13. Roger, I.; Shipman, M.A.; Symes, M.D. Earth-abundant catalysts for electrochemical and photoelectrochemical water splitting. *Nat. Rev. Chem.* **2017**, *1*, 0003. [CrossRef]
14. Du, H.-Y.; Chen, S.-C.; Su, X.-J.; Jiao, L.; Zhang, M.-T. Redox-active ligand assisted multielectron catalysis: A case of Co^{III} complex as water oxidation catalyst. *J. Am. Chem. Soc.* **2018**, *140*, 1557–1565. [CrossRef]
15. Nguyen, A.I.; Darago, L.E.; Balcells, D.; Tilley, T.D. Influence of a "dangling" Co(II) ion bound to a [MnCo$_3$O$_4$] oxo cubane. *J. Am. Chem. Soc.* **2018**, *140*, 9030–9033. [CrossRef] [PubMed]
16. Yin, Q.; Tan, J.M.; Besson, C.; Geletii, Y.V.; Musaev, D.G.; Kuznetsov, A.E.; Luo, Z.; Hardcastle, K.I.; Hill, C.L. A fast soluble carbon-free molecular water oxidation catalyst based on abundant metals. *Science* **2010**, *328*, 342–345. [CrossRef]
17. Martin-Sabi, M.; Soriano-López, J.; Winter, R.S.; Chen, J.-J.; Vilà-Nadal, L.; Long, D.-L.; Galán-Mascarós, J.R.; Cronin, L. Redox tuning the Weakley-type polyoxometalate archetype for the oxygen evolution reaction. *Nat. Catal.* **2018**, *1*, 208–213. [CrossRef]
18. Han, X.-B.; Wang, D.-X.; Gracia-Espino, E.; Luo, Y.-H.; Tan, Y.-Z.; Lu, D.-F.; Li, Y.-G.; Wågberg, T.; Wang, E.-B.; Zheng, L.-S. Fe-substituted cobalt-phosphate polyoxometalates as enhanced oxygen evolution catalysts in acidic media. *Chin. J. Catal.* **2020**, *41*, 853–857. [CrossRef]
19. Azmani, K.; Besora, M.; Soriano-López, J.; Landolsi, M.; Teillout, A.-L.; de Oliveira, P.; Mbomekallé, I.-M.; Poblet, J.M.; Galán-Mascarós, J.-R. Understanding polyoxometalates as water oxidation catalysts through iron vs. cobalt reactivity. *Chem. Sci.* **2021**, *12*, 8755–8766. [CrossRef]

20. Schwarz, B.; Forster, J.; Anjass, M.H.; Daboss, S.; Kranz, C.; Streb, C. From molecular to colloidal manganese vanadium oxides for water oxidation catalysis. *Chem. Commun.* **2017**, *53*, 11576–11579. [CrossRef]

21. Arsalan, M.; Babar, N.-U.-A.; Sadiqa, A.; Mansha, S.; Baig, N.; Nisar, L.; Ashiq, M.N.; Saleh, T.A.; Joya, K.S. Surface-assembled Fe-oxide colloidal nanoparticles for high performance electrocatalytic water oxidation. *Int. J. Hydrogen Energy* **2021**, *46*, 5207–5222. [CrossRef]

22. Trotochaud, L.; Ranney, J.K.; Williams, K.N.; Boettcher, S.W. Solution-cast metal oxide thin film electrocatalysts for oxygen evolution. *J. Am. Chem. Soc.* **2012**, *134*, 17253–17261. [CrossRef]

23. Kanan, M.W.; Nocera, D.G. In situ formation of an oxygen-evolving catalyst in neutral water containing phosphate and Co^{2+}. *Science* **2008**, *321*, 1072–1075. [CrossRef]

24. Wang, J.; Wei, X.; Wang, X.; Song, W.; Zhong, W.; Wang, M.; Ju, J.; Tang, Y. Plasmonic Au nanoparticle@$Ti_3C_2T_x$ heterostructures for improved oxygen evolution performance. *Inorg. Chem.* **2021**, *60*, 5890–5897. [CrossRef]

25. Gutiérrez-Tarriño, S.; Olloqui-Sariego, J.L.; Calvente, J.J.; Palomino, M.; Mínguez Espallargas, G.; Jordá, J.L.; Rey, F.; Oña-Burgos, P. Cobalt metal–organic framework based on two dinuclear secondary building units for electrocatalytic oxygen evolution. *ACS Appl. Mater. Interfaces* **2019**, *11*, 46658–46665. [CrossRef]

26. Zhao, S.; Wang, Y.; Dong, J.; He, C.-T.; Yin, H.; An, P.; Zhao, K.; Zhang, X.; Gao, C.; Zhang, L.; et al. Ultrathin metal–organic framework nanosheets for electrocatalytic oxygen evolution. *Nat. Energy* **2016**, *1*, 16184. [CrossRef]

27. Li, X.; Fang, Y.; Zhao, S.; Wu, J.; Li, F.; Tian, M.; Long, X.; Jin, J.; Ma, J. Nitrogen-doped mesoporous carbon nanosheet/carbon nanotube hybrids as metal-free bi-functional electrocatalysts for water oxidation and oxygen reduction. *J. Mater. Chem. A* **2016**, *4*, 13133–13141. [CrossRef]

28. Lin, Y.; Wu, K.-H.; Lu, Q.; Gu, Q.; Zhang, L.; Zhang, B.; Su, D.; Plodinec, M.; Schlögl, R.; Heumann, S. Electrocatalytic water oxidation at quinone-on-carbon: A model system study. *J. Am. Chem. Soc.* **2018**, *140*, 14717–14724. [CrossRef]

29. Arens, J.T.; Blasco-Ahicart, M.; Azmani, K.; Soriano-López, J.; García-Eguizábal, A.; Poblet, J.M.; Galan-Mascaros, J.R. Water oxidation electrocatalysis in acidic media with Co-containing polyoxometalates. *J. Catal.* **2020**, *389*, 345–351. [CrossRef]

30. Garrido-Barros, P.; Gimbert-Suriñach, C.; Moonshiram, D.; Picón, A.; Monge, P.; Batista, V.S.; Llobet, A. electronic π-delocalization boosts catalytic water oxidation by Cu(II) molecular catalysts heterogenized on graphene sheets. *J. Am. Chem. Soc.* **2017**, *139*, 12907–12910. [CrossRef] [PubMed]

31. Haumann, M. Photosynthetic O_2 formation tracked by time-resolved X-ray experiments. *Science* **2005**, *310*, 1019–1021. [CrossRef] [PubMed]

32. Barber, J. Biological solar energy. *Philos. Trans. R. Soc. A Math. Phys. Eng. Sci.* **2007**, *365*, 1007–1023. [CrossRef]

33. Barber, J. Crystal structure of the oxygen-evolving complex of Photosystem II. *Inorg. Chem.* **2008**, *47*, 1700–1710. [CrossRef]

34. Vogt, L.; Vinyard, D.J.; Khan, S.; Brudvig, G.W. Oxygen-evolving complex of Photosystem II: An analysis of second-shell residues and hydrogen-bonding networks. *Curr. Opin. Chem. Biol.* **2015**, *25*, 152–158. [CrossRef] [PubMed]

35. Wang, Y.N.; Eriksson, L.A. B3LYP studies of the formation of neutral tyrosyl radical Yz and regeneration of neutral tyrosine Yz in PSII. *Int. J. Quantum Chem.* **2001**, *83*, 220–229. [CrossRef]

36. Baranov, S.V.; Ananyev, G.M.; Klimov, V.V.; Dismukes, G.C. Bicarbonate accelerates assembly of the inorganic core of the water-oxidizing complex in manganese-depleted Photosystem II: A proposed biogeochemical role for atmospheric carbon dioxide in oxygenic photosynthesis. *Biochemistry* **2000**, *39*, 6060–6065. [CrossRef] [PubMed]

37. Goberna-Ferrón, S.; Soriano-López, J.; Galán-Mascarós, J. Activity and stability of the tetramanganese polyanion $[Mn_4(H_2O)_2 (PW_9O_{34})_2]^{10-}$ during electrocatalytic water oxidation. *Inorganics* **2015**, *3*, 332–340. [CrossRef]

38. Tandon, S.; Soriano-López, J.; Kathalikkattil, A.C.; Jin, G.; Wix, P.; Venkatesan, M.; Lundy, R.; Morris, M.A.; Watson, G.W.; Schmitt, W. A cubane-type manganese complex with H_2O oxidation capabilities. *Sustain. Energy Fuels* **2020**, *4*, 4464–4468. [CrossRef]

39. Al-Oweini, R.; Sartorel, A.; Bassil, B.S.; Natali, M.; Berardi, S.; Scandola, F.; Kortz, U.; Bonchio, M. Photocatalytic water oxidation by a mixed-valent $Mn^{III}_3Mn^{IV}O_3$ manganese oxo core that mimics the natural oxygen-evolving center. *Angew. Chem. Int. Ed.* **2014**, *53*, 11182–11185. [CrossRef]

40. Brimblecombe, R.; Swiegers, G.F.; Dismukes, G.C.; Spiccia, L. Sustained water oxidation photocatalysis by a bioinspired manganese cluster. *Angew. Chem. Int. Ed.* **2008**, *47*, 7335–7338. [CrossRef]

41. Schwarz, B.; Forster, J.; Goetz, M.K.; Yücel, D.; Berger, C.; Jacob, T.; Streb, C. Visible-light-driven water oxidation by a molecular manganese vanadium oxide cluster. *Angew. Chemie Int. Ed.* **2016**, *55*, 6329–6333. [CrossRef] [PubMed]

42. Haxel, G.B.; Hedrick, J.B.; Orris, G.J.; Stauffer, P.H.; Hendley, J.W., II. *Rare Earth Elements: Critical Resources for High Technology*; U.S. Geological Survey (USGS): Renton, VA, USA, 2002. [CrossRef]

43. Hocking, R.K.; Brimblecombe, R.; Chang, L.Y.; Singh, A.; Cheah, M.H.; Glover, C.; Casey, W.H.; Spiccia, L. Water-oxidation catalysis by manganese in a geochemical-like cycle. *Nat. Chem.* **2011**, *3*, 461–466. [CrossRef] [PubMed]

44. Limburg, J.; Vrettos, J.S.; Liable-Sands, L.M.; Rheingold, A.L.; Crabtree, R.H.; Brudvig, G.W. A functional model for O-O bond formation by the O_2-evolving complex in Photosystem II. *Science* **1999**, *283*, 1524–1527. [CrossRef] [PubMed]

45. Maayan, G.; Gluz, N.; Christou, G. A bioinspired soluble manganese cluster as a water oxidation electrocatalyst with low overpotential. *Nat. Catal.* **2018**, *1*, 48–54. [CrossRef]

46. Ghosh, T.; Maayan, G. Efficient homogeneous electrocatalytic water oxidation by a manganese cluster with an overpotential of only 74 mV. *Angew. Chem. Int. Ed.* **2019**, *58*, 2785–2790. [CrossRef]

47. Soriano-López, J.; Elliott, R.; Kathalikkattil, A.C.; Ako, A.M.; Mulahmetović, M.; Venkatesan, M.; Schmitt, W. Bioinspired water oxidation using a Mn-oxo cluster stabilized by non-innocent organic tyrosine Y161 and plastoquinone mimics. *ACS Sustain. Chem. Eng.* **2020**, *8*, 13648–13659. [CrossRef]

48. Ako, A.M.; Hewitt, I.J.; Mereacre, V.; Clérac, R.; Wernsdorfer, W.; Anson, C.E.; Powell, A.K. A ferromagnetically coupled Mn_{19} aggregate with a record S = 83/2 ground spin state. *Angew. Chem. Int. Ed.* **2006**, *45*, 4926–4929. [CrossRef]

49. Boussac, A.; Rappaport, F.; Carrier, P.; Verbavatz, J.-M.; Gobin, R.; Kirilovsky, D.; Rutherford, A.W.; Sugiura, M. Biosynthetic Ca^{2+}/Sr^{2+} exchange in the Photosystem II oxygen-evolving enzyme of Thermosynechococcus elongatus. *J. Biol. Chem.* **2004**, *279*, 22809–22819. [CrossRef]

50. Chevallot-Beroux, E.; Ako, A.M.; Schmitt, W.; Twamley, B.; Moran, J.; Corinne, B.; Ruhlmann, L.; Mameri, S. Synthesis of new Mn_{19} analogues and their structural, electrochemical and catalytic properties. *Dalton Trans.* **2019**, *48*, 4830–4836. [CrossRef]

51. Xia, H.; Zhu, Y.; Lu, D.; Li, M.; Zhang, C.; Yang, B.; Ma, Y. Ruthenium(II) complexes with the mixed ligands 2,2′-Bipyridine and 4,4′-Dialkyl Ester-2,2′-bipyridine as pure red dopants for a single-layer electrophosphorescent device. *J. Phys. Chem. B* **2006**, *110*, 18718–18723. [CrossRef]

52. Sullivan, B.P.; Salmon, D.J.; Meyer, T.J. Mixed phosphine 2,2′-bipyridine complexes of ruthenium. *Inorg. Chem.* **1978**, *17*, 3334–3341. [CrossRef]

53. Blasco-Ahicart, M.; Soriano-López, J.; Carbó, J.J.; Poblet, J.M.; Galan-Mascaros, J.R. Polyoxometalate electrocatalysts based on earth-abundant metals for efficient water oxidation in acidic media. *Nat. Chem.* **2018**, *10*, 24–30. [CrossRef] [PubMed]

54. Weinberg, D.R.; Gagliardi, C.J.; Hull, J.F.; Murphy, C.F.; Kent, C.A.; Westlake, B.C.; Paul, A.; Ess, D.H.; McCafferty, D.G.; Meyer, T.J. Proton-coupled electron transfer. *Chem. Rev.* **2012**, *112*, 4016–4093. [CrossRef] [PubMed]

55. Abdel-Magied, A.F.; Shatskiy, A.; Liao, R.-Z.; Laine, T.M.; Arafa, W.A.A.; Siegbahn, P.E.M.; Kärkäs, M.D.; Åkermark, B.; Johnston, E.V. Chemical and photochemical water oxidation mediated by an efficient single-site ruthenium catalyst. *ChemSusChem* **2016**, *9*, 3448–3456. [CrossRef] [PubMed]